Article

Study of Co-Doped $K_2Ti_6O_{13}$ Lead-Free Ceramic for Positive Temperature Coefficient Thermistor Applications

Mohammad Shariq [1,*], Mohd Asim Siddiqui [2], Muhammad Azam Qamar [3,*], Y. Altowairqi [4], Syed Kashif Ali [5], Osama Madkhali [1], Mohammed M. Fadhali [1,6], T. Alharbi [7,*], Mohd. Shakir Khan [7,*], Imam Saheb Syed [5], Zeyad M. Ahmed [5] and Majed Yousef Awaji [1,8]

1. Department of Physics, College of Science, Jazan University, Jazan 45142, Saudi Arabia
2. Department of Physics, Shinas College of Technology, Sohar 324, Oman
3. Department of Chemistry, School of Science, University of Management and Technology, Lahore 54770, Pakistan
4. Department of Physics, College of Science, Taif University, P.O. Box 11099, Taif 21944, Saudi Arabia
5. Department of Chemistry, College of Science, Jazan University, Jazan 45142, Saudi Arabia
6. Department of Physics, Faculty of Science, Ibb University, Ibb 70270, Yemen
7. Department of Physics, College of Science, Al-Zulfi, Majmaah University, Al-Majmaah 11952, Saudi Arabia
8. UMR CNRS 7198, Institute Jean Lamour, University of Lorraine, 54011 Nancy, France
* Correspondence: aligshariq@gmail.com (M.S.); qamariub@gmail.com (M.A.Q.); t.alharbi@mu.edu.sa (T.A.); ms.khan@mu.edu.sa (M.S.K.)

Abstract: Cobalt-doped potassium hexa-titanate (Co_x:$K_2Ti_6O_{13}$ (x = 0.05, 0.10, 0.15 mole%)) ceramics were synthesized by the solid-state reaction method. The XRD patterns confirmed single-phase development in a monoclinic symmetry of various samples, and they were used for different structural calculations of Co_x:$K_2Ti_6O_{13}$ ceramics. The dielectric constant, tanδ, electrical modulus, and ac conductivity of Co-doped $K_2Ti_6O_{13}$ were studied in the temperature range of 100–500 °C. Anomalies were observed in graphs of the dielectric constant versus temperature, showing the transition phase in the studied samples. Dielectric peaks at transition temperature decreased with an increasing frequency, and the peaks shifted toward higher temperatures, illustrating the relaxation of the dielectric materials. The composition with x = 0.10 showed low dielectric loss and a higher dielectric constant and can be utilized for high-temperature dielectric material. Small doping of cobalt improved the ac conductivity of $K_2Ti_6O_{13}$ ceramics due to the increase in the spin–phonon interaction and dominant electron hopping conduction; however, the conductivity diminished with substantial doping because of the contraction of the tunnel space and ambushing of conduction electrons. The uniqueness of this study is in the high dielectric optimization of lead-free ceramic Co_x:$K_2Ti_6O_{13}$ and the discovery of positive temperature coefficients of the resistivity of these ceramic samples.

Keywords: alkali titanate; dielectric constant; phase transition; ceramics

1. Introduction

Titanates with the chemical expression $M_2O \cdot nTiO_2$ (where 'M' denotes elements such as Li, Na, K, etc., and n = 2–8) have attracted researchers' interest over the past decade because of their outstanding properties. Depending on the value of 'n', these titanates can have a laminated or tunnel crystal structure comprising octahedral TiO_6, which shares edges with interposing cations. $K_2Ti_2O_5$ and $K_2Ti_4O_9$ structures are made up of layered foils of TiO_5 or TiO_6 octahedra connected to potassium atoms [1]. Especially, potassium titanates, such as $K_2Ti_6O_{13}$, $K_2Ti_2O_5$, and $K_2Ti_4O_9$, are known for their high thermal durability, chemical resistivity, dispersibility, insubstantial metal ion evacuation, and ion exchangers, covering several applications [2]. The photocatalytic activity of long $K_2Ti_6O_{13}$ whiskers synthesized via the traditional sol-gel process was examined for H_2 evolution and CO_2 photoreduction [3]. The photocatalytic efficiency of carbon quantum

dot-modified $K_2Ti_6O_{13}$ composite was examined via amoxicillin degradation under visible light irradiation. [4]. $K_2Ti_6O_{13}$ is also used in metallic supports, such as copper, to improve wear and tear resistance [5]; plastics to improve mechanical and dielectric properties [6]; and car brake lining cushions as a replacement for carcinogenic asbestos [7]. $K_2Ti_6O_{13}$ nanorods were produced and tested as a potassium-ion battery anode material for large-scale energy storage systems [8]. Zhang et al. researched the photocatalytic and antibacterial performance of Cu-doped $K_2Ti_6O_{13}$ nanowires prepared using a combination of sol–gel and hydrothermal methods [9]. In general, alkali titanates are employed as metal ion absorbents, and their cation transfer safeguards the environment from the deadly radiation of exceedingly radioactive fluid squanders [10]. Nanomaterials of titanate also exhibited high performance in gas detection, photovoltaic cells, and cells of high-energy [11]. Water bodies have been effectively cleared of harmful industrial pollutants, including methyl orange and methyl blue, by TiS_3 nanostructures. Using the chemical vapor transport method, J. Singh et al. discovered two-dimensional TiS_3 nanoribbons with outstanding mobility properties, and their photocatalytic activities have been investigated for possible environmental applications [12].

Some alternative advantages of transition metal-doped $K_2Ti_6O_{13}$ over Pb-based perovskite ceramics have been reported previously [13–15]. For instance, by doping divalent Cu^{2+} with $K_2Ti_6O_{13}$ ceramics, generally, charge compensation progress may evolve oxygen vacancies ($V_o^{\bullet\bullet}$, which are assertive charge carriers in ceramics), changing the ligand symmetry around the dopant and ultimately enhancing the dielectric properties of ceramics [14]. Alternatively, in the perovskite lattice, it is believed that acceptor impurities can accelerate dielectric aging and lead to the formation of compensating positively charged $V_o^{\bullet\bullet}$, which can impact device performance [14]. PbO-based ceramics have excellent ferroelectric properties, but the volatile nature of deadly lead oxide during the synthesis process produces environmental pollution and induces inconsistency in composition. Because alkali titanates are Pb-free ceramics and have potential applications in industry, studies on alkali titanates have been encouraged. Various synthesis routes exist to prepare potassium hexa-titanate ($K_2Ti_6O_{13}$), such as the solid-state reaction method, the sol–gel method, the hydrothermal method, etc. Such a variety of preparations could also change alkaline titanate materials by doping them with aliovalent transition metal ions. Vikram et al. described the structural analysis, microtubular particles by SEM micrographs, and ferroelectric–paraelectric-type phase transition of Cu-doped $K_2Ti_6O_{13}$ ceramics [14]. Vikram et al. focused on EPR spectroscopy in another study on $Mn_x:K_2Ti_6O_{13}$ lead-free ceramics, recognizing Mn^{4+}, Mn^{3+}, and Mn^{2+} partial substitutions at Ti^{4+} lattice sites; they identified defective accomplice dipoles exhibited in low-field EPR signals at different Mn doping concentrations [16]. This study is aimed to find the positive temperature coefficient resistivity and temperature dependence dielectric of $Co_x:K_2Ti_6O_{13}$ ceramics for PTC thermistor application, which has not been previously reported according to our literature search. In this work, we report the structural properties and the temperature dependence of the dielectric constant and conductivity, along with an estimation of the ferroelectric phase transition temperature of $Co_x:K_2Ti_6O_{13}$ lead-free ceramics.

2. Experimental Procedures

A traditional mixed-ceramics process was utilized for the preparation of $Co_x:K_2Ti_6O_{13}$ ceramics (x = 0.05, 0.10, and 0.15 mole%) by a solid-state reaction method. Taking Co_3O_4 powder (purity 99.9%, Sigma Aldrich, St. Louis, MO, USA) and granulated K_2CO_3 and TiO_2 powders (purity 99.9%, Sigma Aldrich, St. Louis, MO, USA) in stoichiometric amounts, these reactants were thoroughly ground with acetone in an agate mortar. Co ions replace Ti ions in $Co_x:K_2Ti_6O_{13}$ ceramics. The required weight of $Co_x:K_2Ti_6O_{13}$ (x = 0.05, 0.10, 0.15 mole%) can be calculated from the molecular weight calculations of $K_2Ti_{5.95}Co_{0.05}O_{13}$, $K_2Ti_{5.90}Co_{0.10}O_{13}$, and $K_2Ti_{5.85}Co_{0.15}O_{13}$, respectively. These powders were calcined at a high temperature of 1000 °C for 24 h in a muffle furnace and then naturally cooled in the furnace. Powders of various compositions were pressed at 15 MPa into circular disks with

radiuses of 6.5 mm and thicknesses of 1.00 mm, and the disks were additionally sintered at 1000 °C for 60 min. Figure 1 shows schematic diagram for synthesis of cobalt-doped $K_2Ti_6O_{13}$. XRD patterns of various samples were achieved at room temperature on an X-ray powder diffractometer (Rigaku; Model: SC-30; Cat. No. 5738 E-1, Tokyo, Japan) operating at 100 mA and 40 kV using Cu Ka radiation (k = 1.5418 A°) with a scanning rate of 2 °/min. The dielectric estimations were completed on silver-pasted disk samples for the temperature range of 100 °C to 500 °C at three frequencies—100, 200, and 400 kHz—using the LCR HI-Tester (HIOKI 3532-50, Tokyo, Japan). Direct measurements of the parallel capacitance (C_p) and tangent loss were taken using an impedance analyzer. However, the relationship $\varepsilon_r = C_p/(\varepsilon_o(a/t))$, where t and an are the thickness and cross-sectional area of the pellet, respectively, was used to compute the dielectric constant.

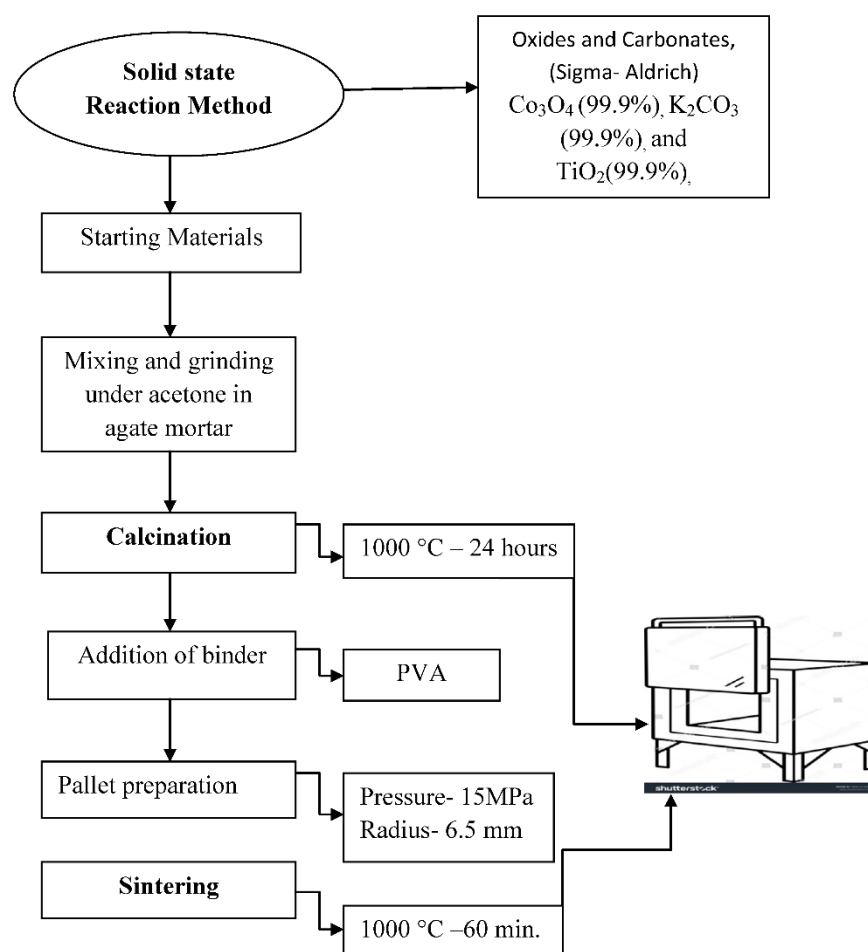**Schematic diagram of synthesis of $Co_x:K_2Ti_6O_{13}$ ceramics**

Figure 1. Schematic diagram of preparation of cobalt-doped $K_2Ti_6O_{13}$.

3. Results and Discussions

Figure 2 demonstrates the XRD patterns of $K_2Ti_6O_{13}$ and cobalt-doped $K_2Ti_6O_{13}$ (x = 0.05, 0.10, and 0.15 mole%, respectively) ceramics at room temperature. The XRD patterns were analyzed to identify the phase and lattice parameters of the samples. The peak positions of all samples were similar, and there were no secondary phases visible in the patterns, indicating that the $K_2Ti_6O_{13}$ matrix appeared in a single phase with Co-doping. The XRD pattern of different samples confirmed the monoclinic structure of $Co:K_2Ti_6O_{13}$ ceramic.
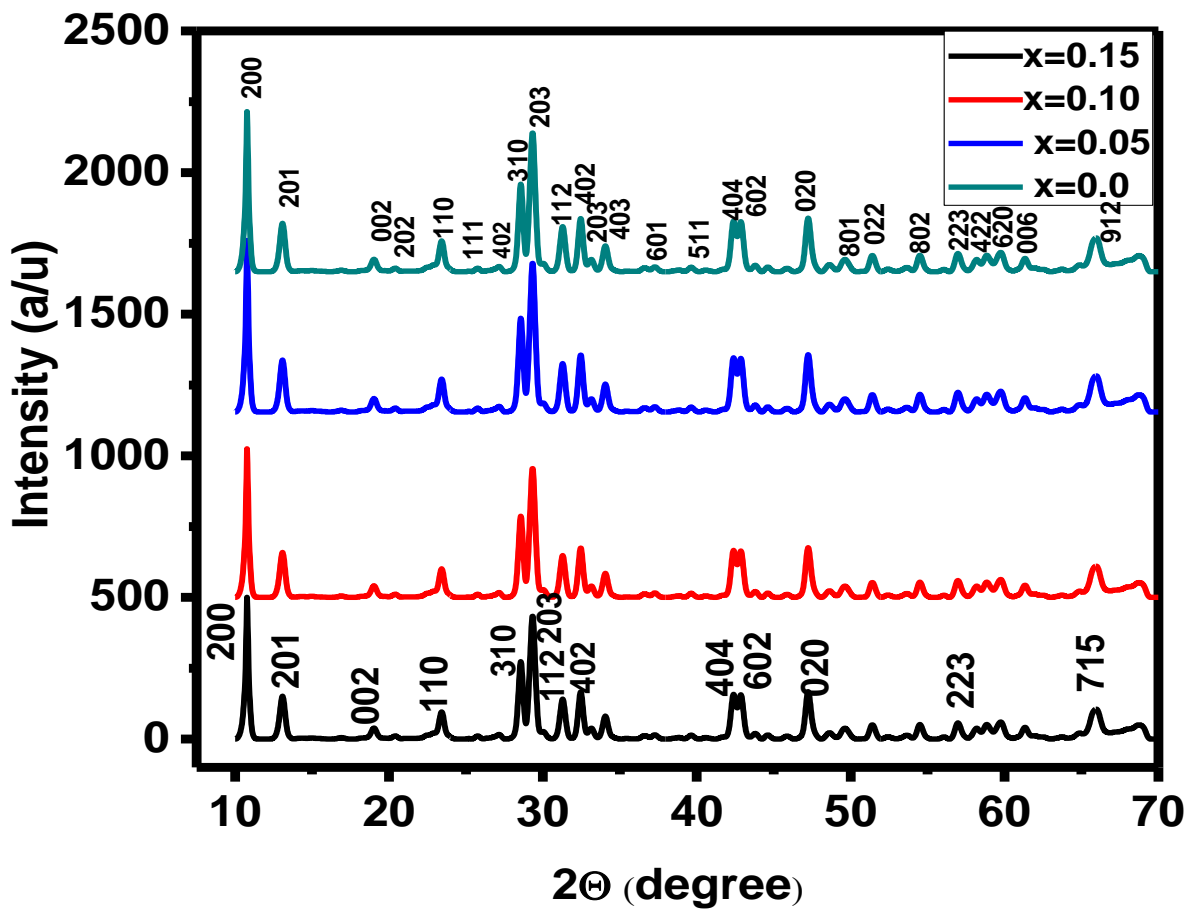
Figure 2. XRD pattern of cobalt-doped $K_2Ti_6O_{13}$ and $K_2Ti_6O_{13}$ ceramics.

The room-temperature lattice constants of $K_2Ti_6O_{13}$ and Co: $K_2Ti_6O_{13}$ ceramics were calculated by [15]:

$$\frac{1}{d_{hkl}^2} = \frac{h^2}{a^2 sin^2\beta} + \frac{k^2}{b^2} + \frac{l^2}{c^2 sin^2\beta} - \frac{2hlcos\beta}{ac\,sin^2\beta} \text{ (Monoclinic)} \tag{1}$$

where d_{hkl} is interplanar distance; h, k, and l are the Bragg plane Miller indices; and β is angular orientation. Various structural parameters are listed in Table 1. The physical size of unit cells in a crystal lattice is referred to as the lattice constant. The lattice parameters of a doped material vary in comparison with the undoped material when a heteroatom with a lower or higher radius is doped in a lattice structure. The size variation of the unit cell is directly influenced by the size of the impure dopant. The variance is further enhanced by the doping percentage. Ti^{4+} has an ionic radius of 0.68 Å, while Co^{2+} has an ionic radius of 0.74 Å. In Co-doped $K_2Ti_6O_{13}$, Ti with a reduced radius is replaced by Co with a slightly larger radius, resulting in an increase in the lattice constant. Table 1 shows the volume of unit cells for various samples. It was observed that increasing the doping percentage consistently increased the unit cell volume, as shown in Figure 3.

Table 1. Various structural parameters of $K_2Ti_6O_{13}$ and $Co_x:K_2Ti_6O_{13}$ ceramics (x = 0.0, 0.05, 0.1, and 0.15 mole%) at room temperature.

X: $K_2Ti_6O_{13}$ (Mole%)	2θ (Deg.)	FWHM (deg.)	D_{hkl} (nm)	$a, b, c,$ Å; $\alpha,$ deg.	Volume of Unit Cell (Å^3)	%C
0	10.779	0.200	127.06	15.570, 3.806, 9.104; 99.568°	531.90	92.3
0.05	10.780	0.199	127.70	15.584, 3.834, 9.116; 99.820°	536.69	94.4
0.1	10.780	0.192	132.45	15.625, 3.834, 9.128; 99.832°	538.74	95.1
0.15	10.780	0.191	133.05	15.647, 3.835, 9.159; 99.854°	541.48	96.2
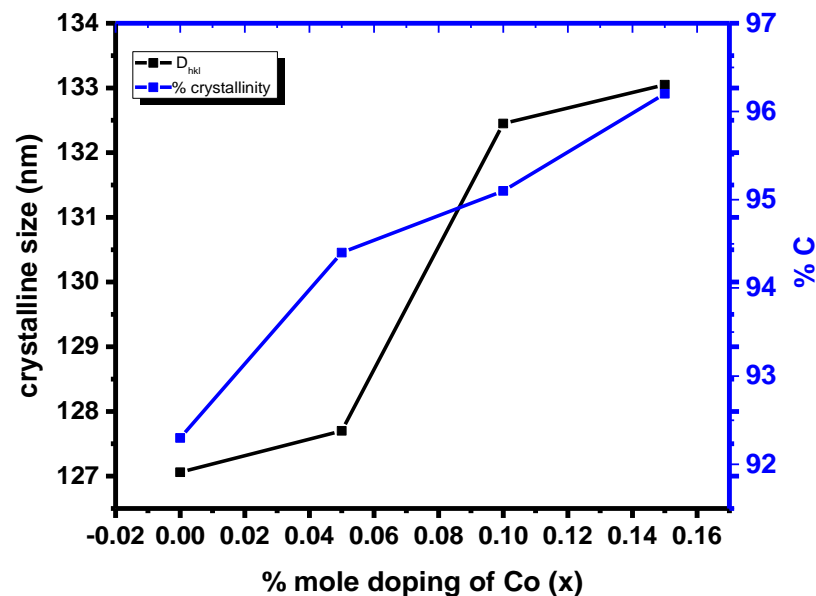
Figure 3. Crystallite size (D_{hkl}) and crystallinity (%C) variations with Co-doping in $Co:K_2Ti_6O_{13}$.

The most apparent peak at θ = (200) may be used to calculate the crystallite size (D_{hkl}) of the identified crystalline phase using an amended Scherrer formula (200) [17–19]:

$$D_{hkl} = \frac{k\lambda}{\beta \ \cos\theta} \tag{2}$$

D_{hkl} denotes the crystalline size, k denotes a dimension free-form factor with a value near unity (0.9), λ is the Cu Kα_1 X-ray wavelength, β is the line broadening (FWHM), and θ is the Bragg angle. The grain size was measured along the (200) peak and found to increase with the amount of Co in the ceramics. Because of the difference in ionic radii between Co^{2+} and Ti^{4+} ions, it was also expected that Co: $K_2Ti_6O_{13}$ would be formed with a large crystalline size due to more agglomeration.

The crystallinity (C) of any sample can be characterized as [20]:

$$\%C = \frac{A_{cryst}}{A_{total}} \times 100 \qquad (3)$$

where A_{cryst} is the total area of all crystalline peaks in an X-ray diffraction pattern, and A_{total} is the total area of the diffraction pattern. Figure 3 exhibits the crystallinity of $Co_x:K_2Ti_6O_{13}$ ceramics as a function of the cobalt substituent concentration. Table 1 shows that the Co-doped $K_2Ti_6O_{13}$ ceramics were slightly more crystalline than $K_2Ti_6O_{13}$, and the crystallinity increased with increasing Co content. The slight elevation in crystallinity was due to the addition of a heavier element, such as Co, in place of Ti.

Figure 4 depicts the variation of the dielectric constant of $Co_x:K_2Ti_6O_{13}$ ceramics with temperature at frequencies of 100, 200, and 400 kHz. It can be seen that the dielectric constant rose with temperature up to a certain critical temperature and then started decreasing with a further increase in temperature. The Curie transition (T_c, ferroelectric–paraelectric type transition) temperature of $K_2Ti_6O_{13}$ ceramics is reported at 300 °C [16]. Dielectric peaks of $Co_{0.05}:K_2Ti_6O_{13}$ were observed at temperatures of 335 °C, 348 °C, and 349 °C for 100 kHz, 200 kHz, and 400 kHz, correspondingly (Figure 4a). The dielectric constant peak at T_c diminished, and the transition temperature moved to a higher value with a rising frequency, showing evidence of the relaxation behavior of the dielectric material [21]. For $Co_{0.10}:K_2Ti_6O_{13}$ ceramic, two ferroelectric–paraelectric peaks appeared at 283 °C (bigger peak, T_{C1}) and 430 °C (smaller peak, T_{C2}). Moreover, $Co_{0.15}:K_2Ti_6O_{13}$ showed a low permittivity transition peak at a comparatively higher temperature of 387 °C, with zero frequency dispersion up to 260 °C, which was almost in the vicinity of the tangent loss peak (Figure 4c). Changes in relaxation time and lattice disorder caused by dopant incorporation could be the cause of the peaks shifting to higher temperatures. It was observed that the dielectric constant of $Co_x:K_2Ti_6O_{13}$ ceramic increased with Co-doping for x = 0.05, 0.10, and then it diminished inevitably for x = 0.15 mole% compared with that of pure $K_2Ti_6O_{13}$ [16]. Because Co^{2+} has greater atomic polarizability than titanium, the dielectric constant of $Co_x:K_2Ti_6O_{13}$ rose with increased Co-doping (where x = 0.05, 0.10). However, at a concentration of x = 0.15, the porosity of the sample increased, which raised the resistivity and made polarization incredibly difficult and may have lowered the dielectric constant. The dielectric peaks observed to broaden and become disordered in the lattice due to Co^{2+} ions may have been responsible for this broadening peak, prompting heterogeneity in the micro-composition. The incorporation of Co^{2+} ions into the lattice induced oxygen vacancies ($V_o^{\bullet\bullet}$), causing distortion of the surrounding volume and adjustment of the local fields. Additionally, a broadening of the peak happens due to non-uniform internal fields resulting from ($Fe–V_o^{\bullet\bullet}$) defect-associated dipoles [22]. The transition temperature and dielectric peak of $Co_x:K_2Ti_6O_{13}$ ceramics at frequencies of 100 kHz, 200 kHz, and 400 kHz are listed in Table 2.

Table 2. Transition temperature and dielectric peak of $Co_x:K_2Ti_6O_{13}$ ceramics at frequencies of 100 kHz, 200 kHz, and 400 kHz.

X: K2Ti6O13 (Mole%)	TC °C (100 kHz)	TC °C (200 kHz)	TC °C (400 kHz)	εr Peak (100 kHz)	εr Peak (200 kHz)	εr Peak (400 kHz)
0.05	335	348	349	128	112	95
0.1	283, 430	282, 430	283, 430	258	139.3	105
0.15	397	385	385	61.9	57	50.6
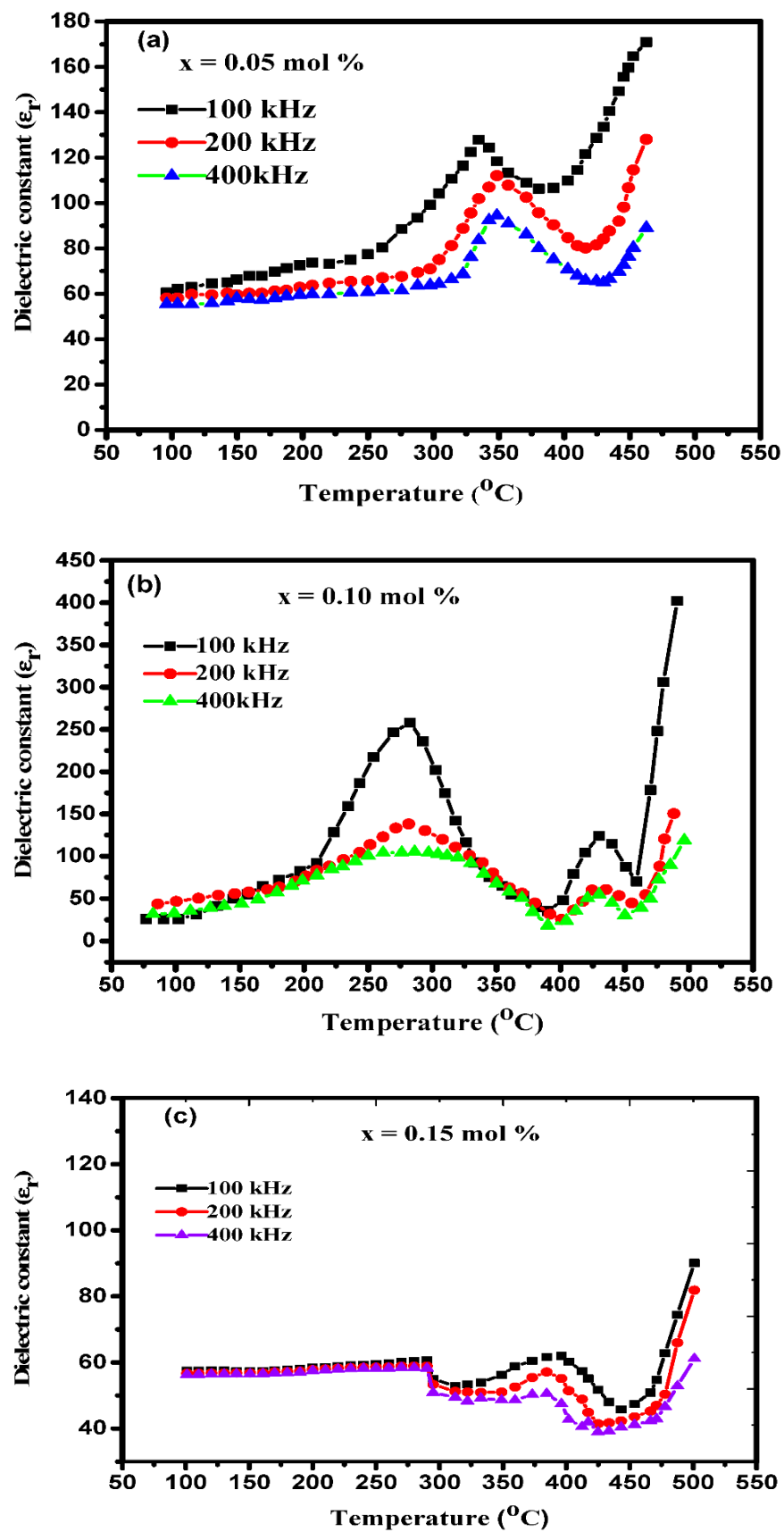
Figure 4. Dielectric constant of $Co_x:K_2Ti_6O_{13}$ ceramics as a function of temperature; (**a**) is for $Co_{0.05}:K_2Ti_6O_{13}$, (**b**) is for $Co_{0.10}:K_2Ti_6O_{13}$ and (**c**) is for $Co_{0.15}:K_2Ti_6O_{13}$.

Figure 5 shows the variation of the dielectric loss of $Co_x:K_2Ti_6O_{13}$ ceramics with temperature at frequencies of 100, 200, and 400 kHz. Dielectric loss was found to rise with temperature up to a certain temperature, and after that, it decreased with an increasing frequency for all doped compositions. Tangent loss peaks of $Co_{0.05}:K_2Ti_6O_{13}$ were observed at temperatures of 335 °C, 340 °C, and 347 °C for 100 kHz, 200 kHz, and 400 kHz, respectively. Herein, the tangent loss peak was moved to a higher temperature, and loss was reduced with increasing frequency, exhibiting ferroelectric relaxation that could be assigned to a reduction in the relaxation time with temperature [23]. For $Co_{0.10}:K_2Ti_6O_{13}$ ceramic, the single ferroelectric–paraelectric peak bifurcated itself into two peaks, which occurred at 283 °C and 430 °C, following a trend similar to that of dielectric permittivity (Figure 5b). However, a single transition peak was subsequently obtained at a temperature of 384 °C for $Co_{0.15}:K_2Ti_6O_{13}$ ceramic. The typical increment in tanδ with temperature might have been because of leakage current and an increase in the number of ions participating in polarization [24]. The high rate of tangent loss at lower frequencies and higher temperatures results from space charge polarization [25]. Compared with $K_2Ti_6O_{13}$ [17], a nearly uniform dielectric loss pattern was obtained in doped $Co_x:K_2Ti_6O_{13}$. The peaks of tangent loss in various doped samples are credited to the homogeneity in the composition because of doping. However, the oxygen vacancies that keep the crystal structure stable also affect mobility in the oxygen sublattice (CoO_6 and TiO_6), acting as fast ion conductors [26]. The origin of the loss peaks is expected to be the relaxation of permanent dipoles and ($Fe–V_o^{\bullet\bullet}$) deformity associated with the dipoles [25]. The dielectric behavior of $Co_x:K_2Ti_6O_{13}$ ceramics near phase transition (Tc) can be explained by utilizing the perovskite material idea, while the phase transition can be ascribed to the instability of the temperature-dependent soft phonon mode (i.e., low-frequency mode), in which the frequency approaches 0 and the corresponding lattice displacements become unstable [23]. The soft mode concept may be used to explain the above properties using the real part of the dielectric constant and tangent loss, which are similar to the Debye equations [27]:

$$\omega_{soft} \propto (T - Tc)^{1/2} \tag{4}$$

and in the range $\omega \ll \Omega_\lambda(q)$.

$$\varepsilon(\omega) = \frac{\left[8\pi N \mu^2 \Omega_\lambda(q)\right]}{\Omega_\lambda^2(q)\left\{1 + \Omega_\lambda^2(q)\tau_\lambda^2(q)\right\}} \tag{5}$$

$$\text{Tan } \delta = \frac{[\Omega_\lambda(q)\tau_\lambda(q)]}{\left\{1 + \Omega_\lambda^2(q)\tau_\lambda^2(q)\right\}} \tag{6}$$

where $\tau_\lambda(q)$ denotes relaxation time and $\Omega_\lambda(q)$ denotes the phonon frequency [28]. Although the over-damped soft phonon mode temperature and dielectric relaxation behavior ended up being practically indistinguishable, the permittivity of the ceramics exhibits an abrupt change at the transition temperature (T_C) when the soft phonon mode damping and relaxation impact were insignificant. Moreover, term $\{1 + \Omega_\lambda^2(q)\tau_\lambda^2(q)\}$ in the denominator of the above expression alters the sharp transition to a rounded hump. The maximum loss and relaxation effect could be attributed to the condition $\Omega_\lambda(q) = 1/\tau_\lambda(q)$. The origin of phase transitions indicating dielectric irregularity originated from the unit cell structure, which is temperature-sensitive, and transformed into a progressively steady structure at a particular transition temperature. When the lattice is not able to relax against lattice stresses, assemblies of TiO_6 are intensely contorted, and Ti^{4+} ions lie at its center of mass in an intact oxygen octahedron, developing permanent dipoles. Generally, these dipoles rearrange themselves toward the applied field, resulting in a substantial polarization influence and, consequently, spontaneous polarization in all compositions. It can be understood from Figure 5 that the variation of tangent loss with temperature shows an extremely large energy loss near transition (but below T_c). Intense molecular thermal vibrations above T_c

destroy spontaneous polarization, bringing decay in permittivity. Thus, the ferroelectric–paraelectric-type phase transition was confirmed by the observed peak of the relative permittivity (ε_r) at T_c.
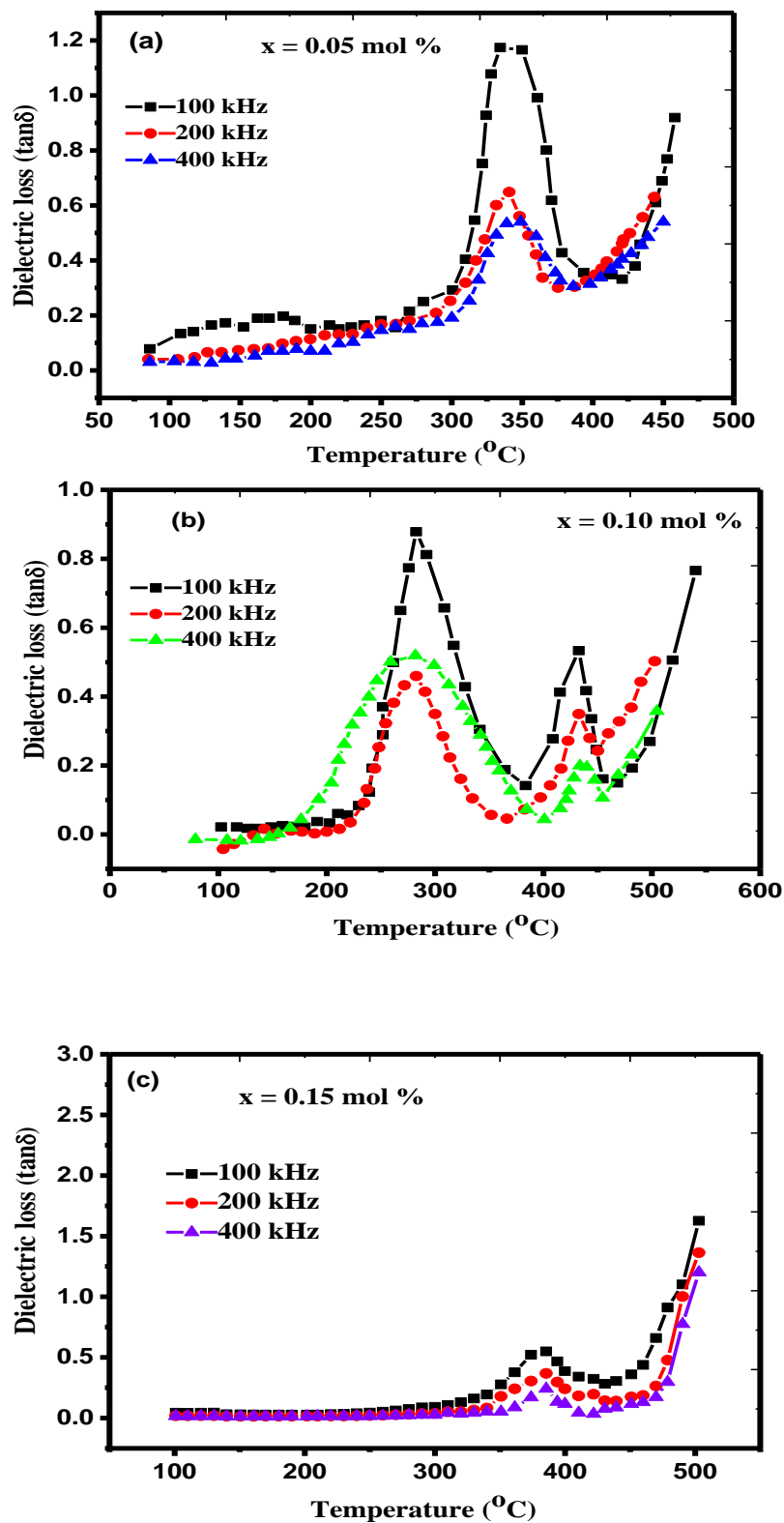

Figure 5. Dielectric loss of Co_x:$K_2Ti_6O_{13}$ ceramics as a function of temperature; (**a**) is for $Co_{0.05}$:$K_2Ti_6O_{13}$, (**b**) is for $Co_{0.10}$:$K_2Ti_6O_{13}$ and (**c**) is for $Co_{0.15}$:$K_2Ti_6O_{13}$.

Figure 6 illustrates the variation of ac conductivity (σ_{ac}) with temperature in the range of 100–500 °C for the frequencies of 100, 200, and 400 kHz. All samples have slightly unusual patterns of ac thermal behavior. On the basis of this behavior, the trend may be divided into four regions for analysis. The activation energy could be determined in different regions using Arrhenius equations [29]:

$$\sigma_{ac} = \sigma_o \exp\left(-\frac{E_a}{kT}\right) \tag{7}$$

$$log\sigma_{ac} = log\sigma_o + \frac{-E_a}{2.30\,kT} \tag{8}$$

where σ_o denotes the pre-exponential factor, E_a denotes activation energy, k denotes the Boltzmann constant, and T denotes absolute temperature. E_a can be calculated by multiplying the Boltzmann constant (0.00008617 eV/K) by the slope of the line.

Region 1 (100–250 °C). The low activation energy region observed in Figure 6 depends on the frequency and temperature of all doped samples, while it slightly depends on temperature. σ_{ac} has the behavior of the Jonscher power law ($\sigma_{ac} = A\omega^s$, where s < 1) and is typically assigned to the hopping motion of electrons [29]. The variation trend of σ_{ac} with temperature was similar for all samples, but slightly more temperature dependence was observed for the x = 0.10 sample. The small incline (slope) in this region showed low activation energy for electric transport.

Region 2 (250–350 °C). In this region of temperature, σ_{ac} strongly depends on temperature and revealed an activation energy value higher than the temperature region below 250 °C, showing the appearance of interchangeable intratunnel ionic conduction. Multiple hops of the hopping electrons are responsible for the temperature dependency of ac conductivity [29] that varies linearly with an improvement in activation energy. Indeed, in this region, the highest activation energy was observed for $Co_{0.10}$:$K_2Ti_6O_{13}$ ceramics.

Region 3 (350–420 °C). Conductivity showed anomalous behavior in this temperature region, showing relaxation peaks at 415 °C (for x = 0.05), 384 °C (for x = 0.10), and 407 °C (for x = 0.15). These relaxation peaks come into existence because of the domination of strong dipole alignment with enhanced doping. The shifting of peaks for different doped samples was due to changes in relaxation time and disorder in the lattice. Conductivity in this area rose to the transition temperature because more conduction electrons are created when an acceptor is ionized. After Tc, conductivity decreased a lot, which may be because the value of mobility goes down as the temperature goes up.

Region 4 (420–500 °C). Conductivity depends strongly on frequency and temperature in this temperature region. The average ac conductivity value in this region again began to increase after a specific temperature above the transition point. The sharp rise in conductivity in this region may have been due to a large increase in intrinsic conductivity, which compensated for the loss in mobility. Grain morphology and grain porosity also have a significant impact on conductivity. The material close to the transition temperature shows a positive temperature coefficient of resistivity (PTCR). The grain boundary is closely related to PTCR behavior [30]. The PTCR effect is caused by trapped electrons at the grain boundaries, as explained by the well-established Heyyang model. The PTCR is a consequence of the dependence of barrier heights on dielectric constants above the transition temperature (T > T_c). The exponential increase in dielectric constants above T_c prompts a reduction in barrier heights and an exponential increase in conductivity. Grain boundary barriers do not have a clear significant role below T_c, and the reduction in barrier height is credited to the remuneration of the grain boundary charge by spontaneous polarization [31]. At the point where the dielectric reduces with temperature, however close to the Tc, the barrier height rises, promoting an increase in resistivity with temperature up to the potential barrier boundary, which is equivalent to the activation energy. Regarding semiconductors, after that temperature, the resistivity begins to diminish with a further rise in temperature. Here, conductivity exhibited a strong temperature dependence and displayed an activation energy value, which is a significant novelty in this study.
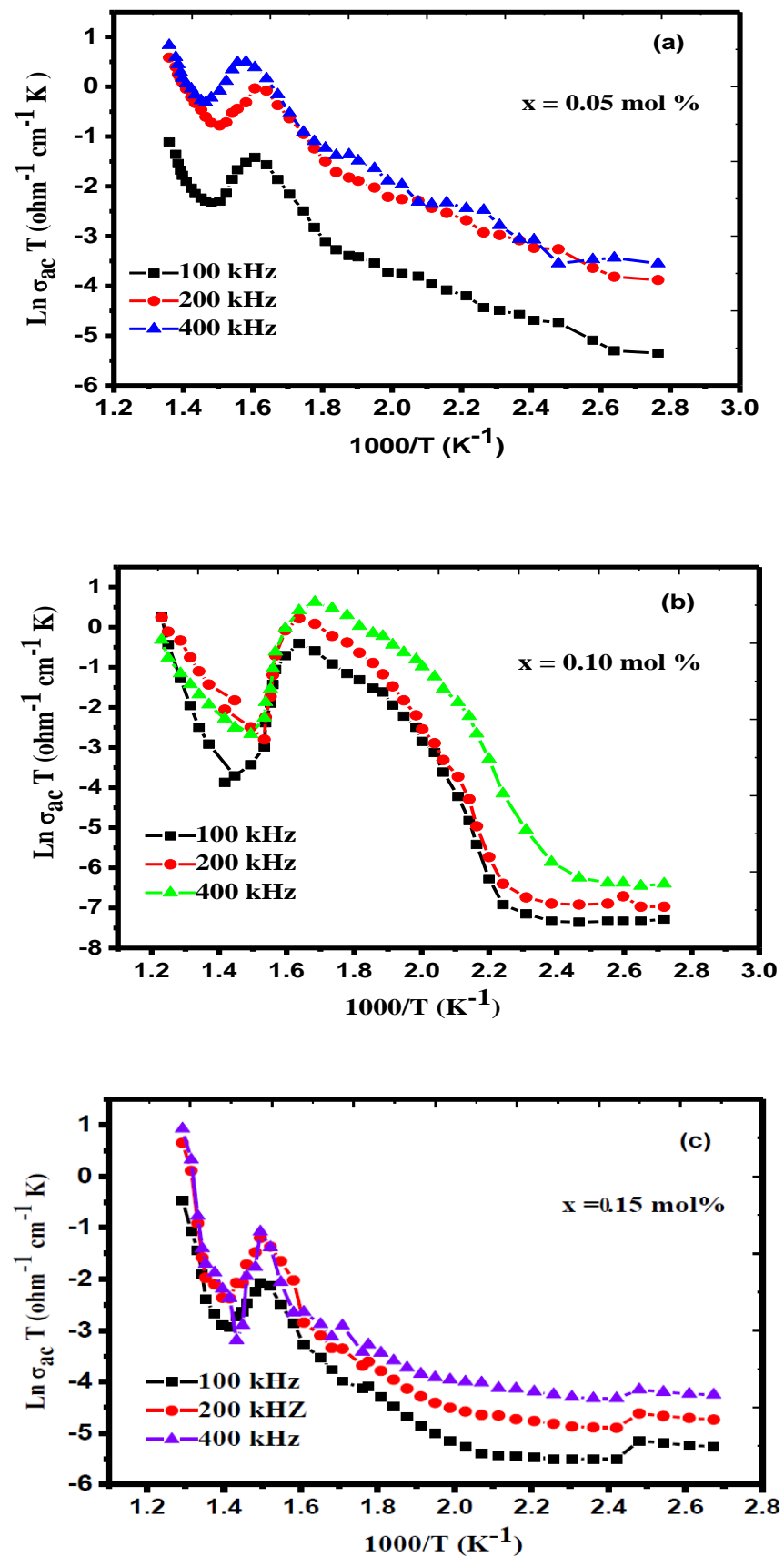
Figure 6. Variation of ac conductivity of $Co_x:K_2Ti_6O_{13}$ ceramics with temperature; (**a**) is for $Co_{0.05}:K_2Ti_6O_{13}$, (**b**) is for $Co_{0.10}:K_2Ti_6O_{13}$ and (**c**) is for $Co_{0.15}:K_2Ti_6O_{13}$.

The complex electric modulus formalism, which is based on polarization analysis, can also be used to evaluate the electrical behavior of materials [32]. The electric modulus may reveal important information about the relaxation mechanism. This method has the benefit of minimizing grain boundary conduction, electrode effects, and the undesirable effects of extrinsic relaxation [33]. The electrical modulus (M*), which is based on the complex permittivity $\varepsilon^* = \varepsilon' - i\varepsilon''$, can be written as follows:

$$M^* = M' - iM'', \text{ where}$$

$$M' = \frac{\varepsilon'}{\varepsilon'^2 + \varepsilon''^2} \text{ and } M'' = \frac{\varepsilon''}{\varepsilon'^2 + \varepsilon''^2}$$

The imaginary and real components of the electrical modulus are M'' and M', respectively. The temperature dependence of real part M' of the electrical modulus at 100 kHz, 200 kHz, and 400 kHz is shown in Figure 7. It was shown that M' decreased with temperature up to a certain temperature, and then it increased again with temperature, resulting in peaks at different temperatures. The values of M' at 400 kHz for all doped samples were higher in almost the entire temperature range. In the higher temperature range, we observed one peak of M' for the x = 0.05- and 0.15-doped samples, and double peaks were observed for the x = 0.10-doped samples. As shown in the dielectric plot in Figure 4, we also observed double peaks for the x = 0.10-doped sample. At very high temperatures, the M' values were close to zero, indicating that electronic polarization was minimal [34].

Figure 8 shows the variation of the imaginary portion of the electrical modulus (M'') with temperature at 100 kHz, 200 kHz, and 400 kHz. It was observed that values of M'' at lower temperatures were lower, and they initially increased with temperature and then decreased, following the exhibition of peaks at higher temperatures. The values of M'' at frequencies of 100 kHz, 200 kHz, and 400 kHz were almost the same for the whole temperature range. M'' started increasing with temperature at lower temperatures for samples x = 0.05 and x = 0.10, whereas it was almost constant up to 225 °C for x = 0.15.
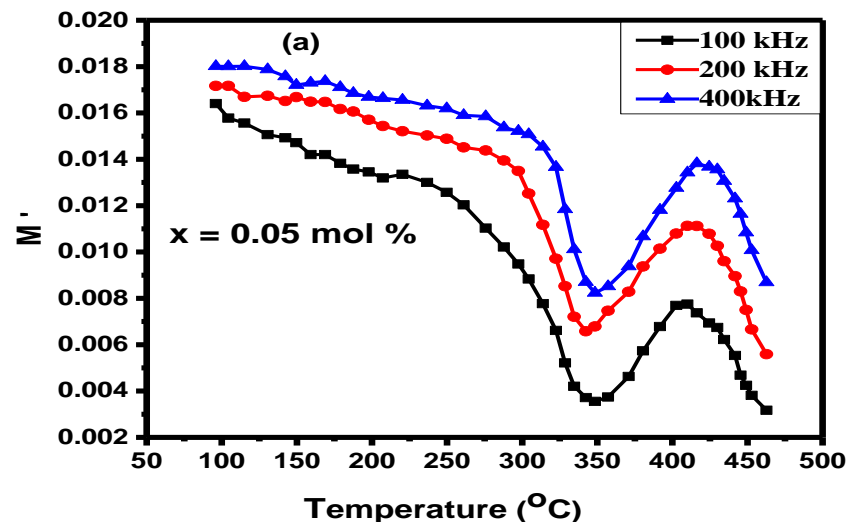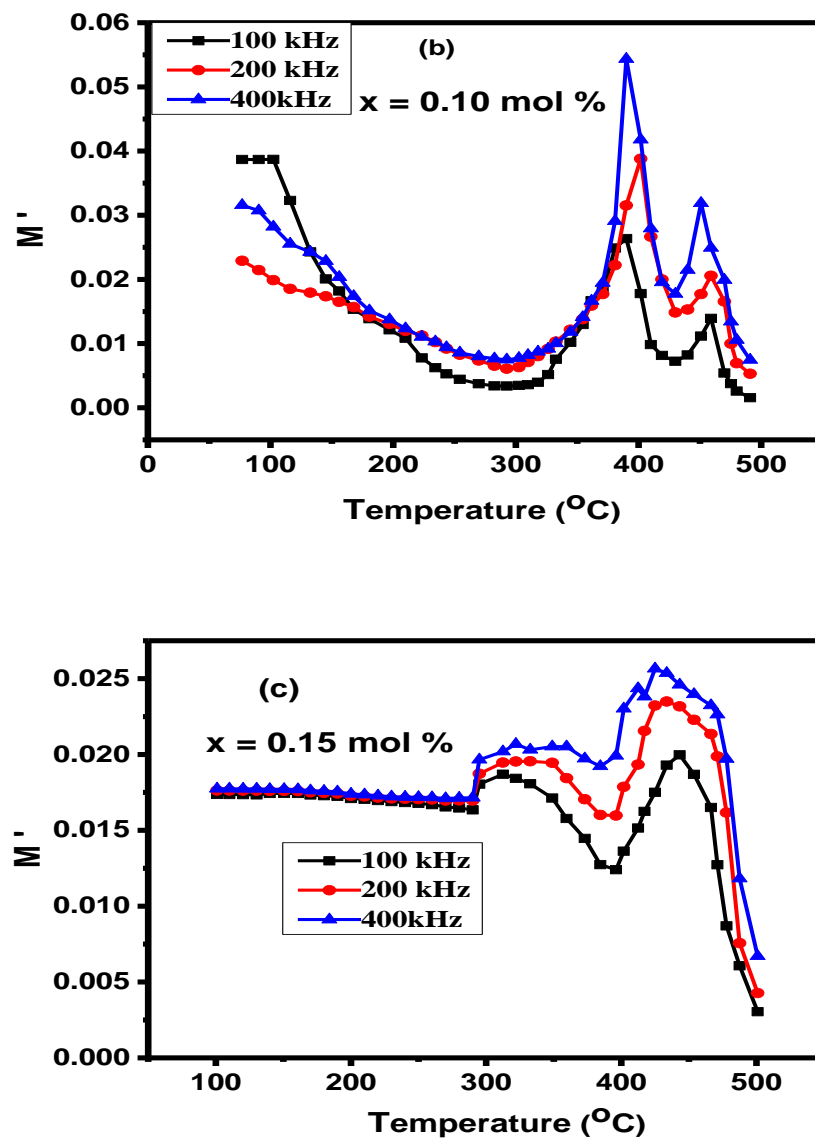

Figure 7. *Cont.*

Figure 7. Variation of M′ of $Co_x:K_2Ti_6O_{13}$ ceramics with temperature at 100, 200, and 400 kHz; (**a**) is for $Co_{0.05}:K_2Ti_6O_{13}$, (**b**) is for $Co_{0.10}:K_2Ti_6O_{13}$ and (**c**) is for $Co_{0.15}:K_2Ti_6O_{13}$.

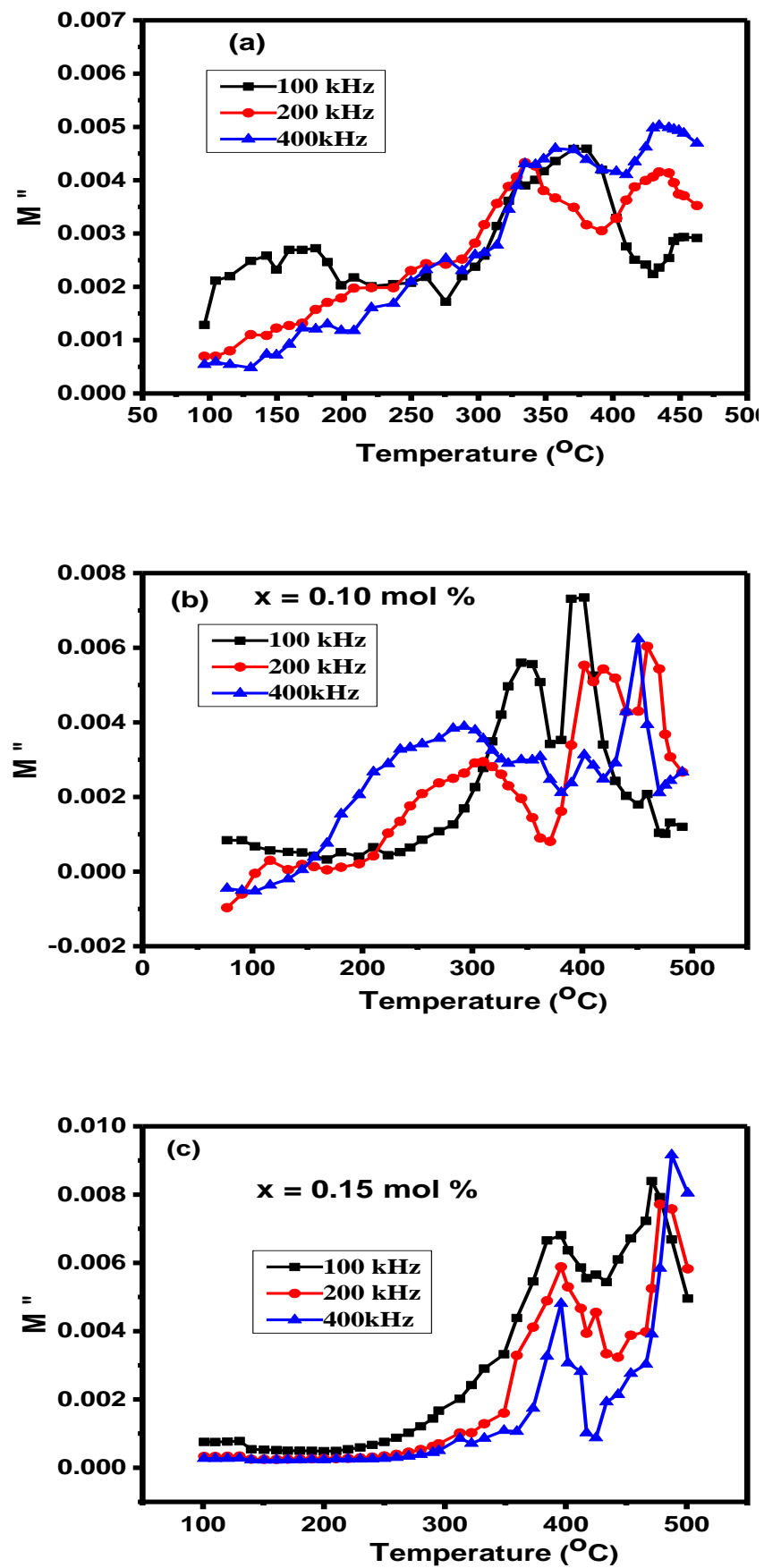**Figure 8.** Variation of M'' of Co_x:$K_2Ti_6O_{13}$ ceramics with temperature at 100, 200, and 400 kHz; (**a**) is for $Co_{0.05}$:$K_2Ti_6O_{13}$, (**b**) is for $Co_{0.10}$:$K_2Ti_6O_{13}$ and (**c**) is for $Co_{0.15}$:$K_2Ti_6O_{13}$.

4. Conclusions

The XRD of the samples verified the production of the $K_2Ti_6O_{13}$ phase with no additional impurity phases. Because of the small difference in the ionic radii of Co^{2+} (0.74 Å) and Ti^{4+} (0.68 Å) ions, the lattice constants and unit cell volume increased slightly with substituent Co content. The dielectric constant changed with temperature, indicating a ferroelectric-to-paraelectric transition, while the Tc value shifted to a somewhat higher temperature, having a higher peak value with increased dopant in the ceramics. The thermal response of the dielectric loss exhibited relaxation peaks at various temperatures, which were attributed to dipole relaxation in almost all chosen compositions. $Co_{0.10}:K_2Ti_6O_{13}$ ceramic was found to have the highest dielectric constant and minimum tangent loss among various samples. The ac conductivity graphs showed that at low temperatures, electronic conduction (via electron hopping) predominated, and at high temperatures, ionic (intratunnel) conduction contributed. The temperature dependence of ac conductivity was greatest between 420 °C and 500 °C.

Author Contributions: Conceptualization, M.A.S.; methodology, M.A.S., M.S.; software, O.M.; validation, M.A.Q., and I.S.S.; formal analysis, Z.M.A.; investigation, M.A.S. and S.K.A.; resources, M.Y.A.; data curation, T.A.; writing—original draft preparation, M.A.S.; writing—review and editing, M.S.; visualization, M.M.F.; supervision, M.S.; project administration, M.S.K.; funding acquisition, Y.A. All authors have read and agreed to the published version of the manuscript.

Institutional Review Board Statement: Not Applicable.

Informed Consent Statement: Not Applicable.

Data Availability Statement: Not Applicable.

Conflicts of Interest: The authors declare no conflict of interest.

References

1. Siddiqui, M.A.; Chandel, V.S.; Azam, A. Comparative study of potassium hexatitanate ($K_2Ti_6O_{13}$) whiskers prepared by sol–gel and solid state reaction routes. *Appl. Surf. Sci.* **2012**, *258*, 7354–7358.
2. Tan, S.; Zhang, Y.; Gong, H. Investigation on K2Ti4O9 Whisker Absorbent and Applications in Heavy Metal Ions Removal. *J. Water Environ. Technol.* **2007**, *5*, 13–18. [CrossRef]
3. Garay-Rodríguez, L.F.; Torres-Martínez, L.M.; Moctezuma, E. Photocatalytic performance of $K_2Ti_6O_{13}$ whiskers to H_2 evolution and CO_2 photo-reduction. *J. Energy Chem.* **2019**, *37*, 18–28.
4. Chen, Q.; Chen, L.; Qi, J.; Tong, Y.; Lv, Y.; Xu, C.; Ni, J.; Liu, W. Photocatalytic degradation of amoxicillin by carbon quantum dots modified $K_2Ti_6O_{13}$ nanotubes: Effect of light wavelength. *Chin. Chem. Lett.* **2019**, *30*, 1214–1218. [CrossRef]
5. Murakami, R.; Matsui, K. Evaluation of mechanical and wear properties of potassium acid titanate whisker-reinforced copper matrix composites formed by hot isostatic pressing. *Wear* **1996**, *201*, 193–198. [CrossRef]
6. Yu, D.; Wu, J.; Zhou, L.; Xie, D.; Wu, S. The dielectric and mechanical properties of a potassium-titanate-whisker-reinforced PP/PA blend. *Compos. Sci. Technol.* **2000**, *60*, 499–508. [CrossRef]
7. Choy, J.H.; Han, Y.S. A combinative flux evaporation–slow cooling route to potassium titanate fibres. *Mater. Lett.* **1998**, *34*, 111–118. [CrossRef]
8. Fegade, U.; Jethave, G.; Khan, F.; Al-Ahmed, A.; Karmouch, R.; Shariq, M.; Inamuddin; Ahmer, M.F. Recent development of aqueous zinc-ion battery cathodes and future challenges: Review. *Int. J. Energy Res.* **2022**, *46*, 13152–13177. [CrossRef]
9. Zhang, W.; Wang, X.; Ma, Y.; Wang, H.; Qi, Y.; Cui, C. Enhanced Photocatalytic and Antibacterial Activities of $K_2Ti_6O_{13}$ Nanowires Induced by Copper Doping. *Crystals* **2020**, *10*, 400. [CrossRef]
10. Kikkawa, S.; Koizumi, M. *Fine Ceramics*; Saito, S., Ed.; Elsevier: Cambridge, MA, USA, 1988; pp. 83–90.
11. Lee, H.K.; Shim, M.J.; Kim, S.W. The characteristics of synthesized potassium hexatitanate and the manufacturing process of the matrix. *Mater. Chem. Phys.* **1996**, *45*, 243–247. [CrossRef]
12. Singh, J.; Sharma, P.; Tripathi, N.; Shishkina, D.; Rymzhina, A.; Boltov, E.A.; Platonov, V.; Pavelyev, V.; Volkov, V.S.; Arsenin, A.V.; et al. Synthesis of highly sensitive nanomaterial for ultra-fast photocatalytic activity: A detailed study on photocatalytic capabilities of rod-shaped TiS3 nanostructures. *Catal. Commun.* **2022**, *162*, 106381. [CrossRef]

13. Wang, B.L.; Chen, Q.; Wang, R.H. Synthesis and characterization of $K_2Ti_6O_{13}$ nanowires. *Chem. Phys. Lett.* **2003**, *376*, 726–731. [CrossRef]

14. Vikram, S.V.; Phase, D.M.; Chandel, V.S. Synthesis, characterization, and electrical studies on Cu-doped $K_2Ti_6O_{13}$ lead-free ceramics: Role of defect associate dipoles. *J. Alloys Compd.* **2010**, *489*, 700–707. [CrossRef]

15. Siddiqui, M.A.; Chandel, V.S.; Shariq, M.; Azam, A. FTIR and dielectric studies of nickel doped potassium hexa-titanate $K_2Ti_6O_{13}$) fine ceramics. *J. Mater. Sci. Mater. Electron.* **2013**, *24*, 4725–4731. [CrossRef]

16. Vikram, S.V.; Phase, D.M.; Chandel, V.S. High-T C phase transition in $K_2Ti_6O_{13}$ lead-free ceramic synthesised using solid-state reaction. *J. Mater. Sci. Mater. Electron.* **2010**, *21*, 902–905. [CrossRef]

17. Shariq, M.; Kaur, D.; Chandel, V.S.; Jain, P.K.; Florence, S.; Sharma, M.; Hussain, S. Study of Structural, Magnetic and Optical Properties of $BiFeO_3$-$PbTiO_3$ Multiferroic Composites. *Arab J. Sci. Eng.* **2019**, *44*, 613–621. [CrossRef]

18. Shariq, M.; Kaur, D.; Chandel, V.S. Structural, magnetic and optical properties of mulitiferroic $(BiFeO_3)_{1-x}(BaTiO_3)_x$ solid solutions. *Chin. J. Phys.* **2017**, *55*, 2192–2198. [CrossRef]

19. Sowjanya, M.; Shariq, M.; Pilli, S.R.; Khan, M.S.; Alharbi, T.; Chaudhary, A.A.; Pamu, D.; Chowdharuy, R.; Fathy, A.M.; Slimani, Y.; et al. Impact of Ar:O2 gas flow ratios on microstructure and optical characteristics of CeO_2-doped ZnO thin films by magnetron sputtering. *EPL* **2021**, *135*, 67003. [CrossRef]

20. Shariq, M.; Imran, M.; Gouda, E.S.; Ansari, A.R.; Siddiqui, M.A.; Sowjanya, M. Study of Structural, Magnetic, Dielectric Properties and Estimation of Magnetoeletric Coupling of La, Mn co-doped $Bi_{1-x}La_xFe_{0.97}Mn_{0.03}O_3$ Ceramics. *Arab J. Sci. Eng.* **2020**, *45*, 475–482. [CrossRef]

21. Li, Z.F.; Wang, C.L.; Zhong, W.L.; Li, J.C.; Zhao, M.L. Dielectric relaxor properties of $K_{0.5}Bi_{0.5}TiO_3$ ferroelectrics prepared by sol–gel method. *J. Appl. Phys.* **2003**, *94*, 2548. [CrossRef]

22. Lines, M.E.; Glass, A.M. *Principles and Applications of Ferroelectrics and Related Materials*; Clarendon: Oxford, UK, 1977; Volume 87, p. 286.

23. Lingwal, V.; Semwal, B.S.; Panwar, N.S. Dielectric properties of $Na_{1-x}K_xNbO_3$ in orthorhombic phase. *Bull. Mater. Sci.* **2003**, *26*, 619–625. [CrossRef]

24. Bogoroditsky, N.P.; Pasynkov, V.V.; Tareev, B. *Electrical Engineering Materials*; Chapters 1 and 3; Mir Publishers: Moscow, Russia, 1979.

25. Das, B.P.; Chaudhary, R.N.P.; Mahapatra, P.K. Effect of Europium (Eu) on structural, dielectric and electrical properties of Pb (SnTi) O3 ferroelectric ceramics. *Mater. Sci. Eng. B* **2003**, *104*, 96–105. [CrossRef]

26. Dwivedi, R.K.; Kumar, D.; Prakash, O. Dielectric relaxation in valence compensated solid solution $Sr_{0.65}La_{0.35}Ti_{0.65}Co_{0.35}O_3$. *J. Phys. D* **2000**, *33*, 88–95. [CrossRef]

27. Vikram, S.V.; Maurya, D.; Phase, D.M.; Chandel, V.S. Effect of defect dipoles on the dielectric and electrical properties of Mn: K2Ti6O13 lead-free ceramics: EPR spectroscopy-cum-dielectric-spectroscopy. *J. Mater. Sci. Mater. Electron.* **2012**, *23*, 718–727. [CrossRef]

28. Goodman, G.; Reynolds, T.G. *Ceramic Materials for Electronics*; Buchanan, R.C., Ed.; Marcel Dekker: New York, NY, USA, 1991; pp. 32–33.

29. Oumezzine, E.; Hcini, S.; Rhouma, F.I.H.; Oumezzine, M. Frequency and temperature dependence of conductance, impedance and electrical modulus studies of $Ni_{0.6}Cu_{0.4}Fe_2O_4$ spinel ferrite. *J. Alloys Compd.* **2017**, *726*, 187–194. [CrossRef]

30. Maurya, D.; Chand, P. On the dielectric spectroscopy of copper doped layered $Na_{1.6}K_{0.4}Ti_3O_7$ ceramics. *J. Alloys Compd.* **2008**, *459*, 418. [CrossRef]

31. Goodman, G. Electrical Conduction Anomaly in Samarium-Doped Barium Titanate. *J. Am. Ceram. Soc.* **1963**, *46*, 48–54. [CrossRef]

32. Heywang, W. Structural engineering of ferroelectrics. *Ferroelectrics* **1983**, *49*, 3–14. [CrossRef]

33. Kaiser, M. Electrical conductivity and complex electric modulus of titanium doped nickel–zinc ferrites. *Phys. B* **2012**, *407*, 606. [CrossRef]

34. Wang, P.G.; Fan, C.M.; Wang, Y.W.; Ding, G.Y.; Yuan, P.H. A dual chelating sol–gel synthesis of BaTiO3 nanoparticles with effective photocatalytic activity for removing humic acid from water. *Mater. Res. Bull.* **2013**, *48*, 869–877. [CrossRef]